E217 STYX

February 6, 2020

The Straw Tube Young student eXperiment (STYX) comprises elements of the forward tracking system of the decommissioned ZEUS detector at DESY. By designing a new trigger and readout system it was converted into a lab course experiment. The aim of STYX is to learn about basic nuclear electronics instrumentation, gas detectors, cosmic radiation, tracking of charged particles and state-of-the art readout systems as well as computer based data analysis.

1. Literature

In preparation for the experiment, we recommend the following literature:

- STYX instructions. Pick up a copy from the tutor!
- Leo, W.R.: Techniques for Nuclear and Particle Physics Experiments
- Grupen, Claus: Astroparticle Physics

There is also an exhaustive overview about cosmic rays in the PDG (although the other references are probably easier to understand):

- PDG chapter 24: Cosmic rays `http://pdg.lbl.gov/2011/reviews/rpp2011-rev-cosmic-rays.pdf`

2. Prerequisites

- Essential for the conduction of the experiment is a solid knowledge of the working principle of gas detectors (chapters 6.1 - 6.5 and 6.7 of the Leo) and of secondary cosmic rays (chapter 7 of the Grupen).
- In general we also expect knowledge on the basics of general particle physics. If you need to refresh your knowledge, just any overview book is OK (e.g. Perkins, Griffiths, ...).

- You should understand the basic working principles of scintillation detectors and photomultipliers. The level of knowledge required for other lab course experiments is sufficient. In case of no prior knowledge, a good introduction can be found in chapters 7.1, 7.2 and 8 of the book by Leo.

- Finally you should be familiar with basic concepts of electronic signal processing. Units used in the setup are amplifiers, shapers, discriminators, TDCs, counters and coincidence units. Information can again be found in chapters 14 and 17 of the book by Leo.

3. Setup

The setup of the experiment is shown in figure 1. The heart of the experiment is the modules which are simple drift chambers. Since the detectors do not have internal trigger system, an external trigger system is used. Beside the modules (copper colored structure) and trigger system (two black panels) different electronic devices are needed to convert the data gathered by the detector and send to the computer for further analysis.

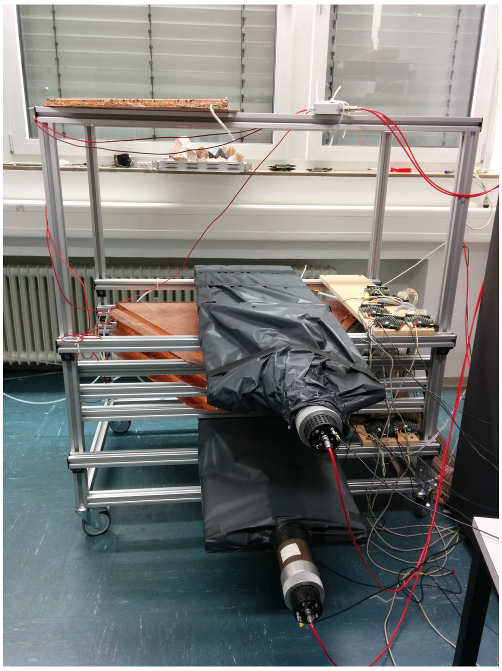

Figure 1: STYX setup with scintillators with attached PMTs (black panels) and the modules (copper colored triangles).

Each module has three layers of 88 straws. The straws are cylinders filled with a gas mixture of argon and carbon dioxide. The radius of the straw tube is 3.75 mm. The length of the straws differ as the module has a triangular form. The shortest straws are 20 cm long and the longest are 102 cm. Each straw is connected to a readout channel in a front-end board. This front-end board contains a preamplifier, a shaper and a discriminator. Figure 2 shows the connecting scheme of the components.

4. Trigger System

The trigger system comprises two large scintillator panels which are mounted above and below two tracking modules. Attached to the scintillating material are photomultiplier tubes (PMTs) which register photons emitted by the material when ionized by passing charged particles. The PMTs convert the very faint light signal into a measurable electronic pulse. Details on the operating principle of PMTs are part of various other lab course experiments.

The panels are operated in a coincidence logic to trigger events where a muon is passing both panels and hence the tracking modules. The electronics setup follows the description in Leo, W.R.: Techniques for Nuclear and Particle Physics Experiments; Chapter 15.4. A readout cycle is triggered if both panels register a hit within a narrow time frame. The timing and the electronics are already set up for you so you don't have to touch anything there. The signals of both panels are adjusted in a way coinciding events result in coinciding signals which are in term fed to the readout system.

However the optimal operating voltage for the PMTs is still to be determined.

5. Front-End Electronics

Front-End electronics (FE) comprises all signal processing that happens close to the physical detector and provides electronic signals which are transfered from the detector to the data acquisition system which can in real life experiments be as far as hundreds of meters from the actual detector. Due to the heritage of STYX basically all elements of modern FE can be found and are used to acquire the data for analysis.

5.1. Details of the STYX readout electronics

Figure 2 gives an overview over the Full readout electronics for the STYX modules.

Most of the FE electronics is housed on three boards directly attached to the detector modules. The initial data processing is done on "ASDQ" chips which each provide amplifiers, shapers and discriminators for eight straws. Simply speaking for each straw a digital output pulse is issued as soon as the input voltage exceeds a given threshold. The output pulses of six straws each are time-multiplexed i.e. the signals are added with 200 ns offset with respect to each other. Thus six output channels are condensed into one at the cost of having a 1200 ns readout window per event.

The FE boards need supply voltage and a reference voltage for the discriminators in the ASDQ. Bot are supplied by external power supplies. They are fed to the FE via so called driver boards which stabilize and filter the original supplied voltages.

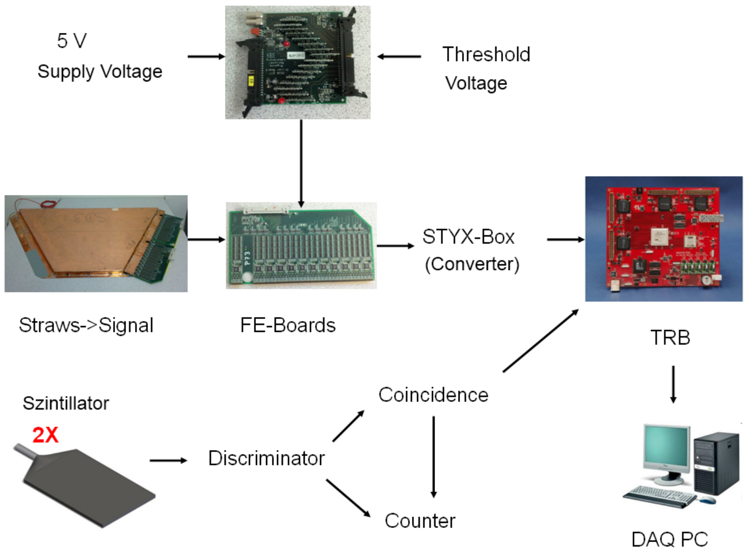

Figure 2: Schematics of the readout electronics for STYX. A detailed description can be found in section 5.1.

6. Data Acquisition and Readout

The signal from the FE board (see section 5.1) is converted in two steps and then fed to the "TRB" TDC board. Here the exact time of the rising and falling edges of the signal pulses as well as the trigger pulse provided by the coincidence of the two scintillation counters is measured with a 100 ps resolution. The recorded data is then streamed to the PC in the lab where it is stored.

The raw data has to undergo some processing steps before being usable as input for further analysis:

- Measured times of leading and trailing edges have to be merged to "hits". The difference of the times for leading and trailing gives the width of a pulse.
- Only pulses which have a width compatible with the expected pulse length (set in the ASDQ) are considered ("cleaning").
- All measured times have to be taken relative to the time of the trigger signal ("reference time").
- Channels of the readout TDC have to be "mapped" to physical locations on the STYX modules where they originate from.
- The position of a time measurement in the acquired signal has to be translated into a single straw position ("demultiplexing").

7. Tasks

7.1. Day 1 – Setup of the experiment

7.1.1. First checks

Before you start, make sure the gas system is working properly (the bubbler at the window should show a bubble every few seconds). The tutor will have enabled the gas system already and turned on the power of all needed electronics components.

7.1.2. PMT operation voltage determination

Ask the assistant to bring up the software for controlling the PMT high voltage and to explain to you how to use it. Make yourself familiar with the different options and how to operate the software.

Only change the values indicated by the assistant. Don't exceed a voltage of 2400 V. If something is not clear, don't hesitate to ask. Faulty operation of the high voltage can result in serious and expensive damage to the experiment.

As a guideline for finding the correct operating voltage, three counters are installed in the electronics rack. The leftmost counter shows the rate for the top panel, the middle counter shows the rate for the bottom panel and the rightmost counter shows the coincidence rate. All values are in hits per 10 seconds.

Note: While in general it is entirely up to you how to evaluate your findings, past experience showed that this task is easiest to do using a spreadsheet application like MS Excel or libreoffice calc (which is available on the machine at the lab course).

- Vary the voltage for the bottom panel between 1700 V and 2300 V in steps of 50 V. Average the observed rate for that panel over several measurements to reduce the statistical uncertainty. With rising voltage you should first observe an exponential and later a linear rise. A good working point is in the beginning of the linear part of the distribution.

- Now vary the voltage of the top panel in the same range. This time look at the coincidence rate. As before, take several measurements per voltage setting to reduce the statistical uncertainty. You should find a clear plateau in which the count rate is largely independent of the applied voltage.

- Discuss your findings and the values you want to choose with the assistant before you continue. Then set the chosen working points and continue with the threshold determination of the straw tube modules.

7.1.3. Determination of the front-end threshold voltage

Now the optimal voltage setting for the front-end chip is to be determined. The voltage is adjusted using the power supply on the table. The voltage can be read off from the built-in gauge. Note that the voltage selected on the power supply does not directly translate into a voltage level of the detector pulses due to signal processing in the FE chips and the threshold voltage stabilization on the driver boards. However a linear correspondence between the set voltage and a pulse height from the straws can be assumed.

- Vary the voltages from 1.4 V to 2.6 V in steps of 0.4 V. For each voltage take 25 000 events. Process the data files with StyxM2C2 using all process steps except for the cleaning. A typical call would be

  ```
  StyxM2C2 -N 25000 -O TS_14V.txt --all --no-clean
           -I /home/styx/data/etraxp114/te13085163152.hld
  ```

  You can find more options on StyxM2C2 in the appendix A.1. This way you should end up with four different monitoring files for the four threshold settings.

- To find good channels which you can use for the next step, produce a monitoring root file for one of your measurements by calling e.g.

  ```
  StyxMonitor TS_14V_mon.txt
  ```

- Compare the measurements for one TDC number and one channel number using StyxThresholdScan, e.g. by calling:

  ```
  StyxThresholdScan 1 5 TS_14V_mon.txt TS_18V_mon.txt
                        TS_22V_mon.txt TS_26V_mon.txt
  ```

  This would compare channel 5 of TDC 1. The channel number can be read off the x-axis of the plot. You can find the full syntax on StyxThresholdScan in appendix A.3.

- What do you observe in the overlay file? Explain what you see! Which threshold voltage would you choose based on your observation?

- Take a look at the rate file. It shows the number of events with a hit in your chosen channel for the different files. Does this back up your choice of the threshold voltage?

- Compare with some other channels from different TDC numbers. Does your choice of operating voltage work for them as well?

- Produce another monitoring root file for the working point you chose. If you chose a voltage in between the values already measured you have to acquire a new dataset of 25 000 events for that setting first.

- Open the resulting ROOT files and carefully look at the overview distributions. Compare "your" file with the file for the lowest threshold setting. Do you see the effect of the threshold? Do all channels look OK or do you spot any problem? You can redo the previous step for any channel you consider problematic and verify your choice.

7.1.4. Calibration

The signals coming from the FE-Boards have different time delays which need to be corrected. There are also noisy or dead straws which should not be considered in the analysis. Therefore, a calibration is necessary. There are two possible options for calibrating the data. **Calibration Option I** (sections 7.1.5 and 7.2.1) uses a pulse generator while **Calibration Option II** (section 7.2.2) uses cosmic data.

7.1.5. Calibration Option I: Pulse data taking and calibration

For the calibration the pulse data should be taken. There is a pulse generator in the crate next to the HV modules. It generates a pulse with fixed settings that should not be changed. When applying StyxM2C2 to the raw data the `--no-merge` option should be used.

- Find the pulse with the scope first directly from the generator, then after the fan-out. The pulse should be stable.
- When taking pulse data you also should trigger with the pulse itself, your tutor will set it up for you.
- Configure TRB for pulse data taking using the icon for test pulses on the monitor.
- Take at least 50 000 events.
- Process the pulse data file with StyxM2C2 using the option `--pulse`, e.g.

```
StyxM2C2 -N 50000 -O pulse.txt --pulse
-I /home/styx/data/etraxp114/te31415926535.hld
```

- Look at the monitoring root files and discuss what you see.

Now you can perform the calibration with the pulse data you took.

- Perform the calibration using the StyxCalibration tool with algorithm CalibPulse, which is described in appendix A.4 for 30 000 events.
- Open the ROOT output file and have a look at the drift time distributions in **Uncalibrated/Straws**. What do you see?
- Now look at the two-dimensional plots in the directory **Uncalibrated/Layers2D**. Describe what you see. What do you guess is shown in this histogramms?

- Now have a look at the histograms in the directories **Calibrated/Straws** and **Calibrated/Layers2D**. What changed in the distributions?
- Save example plots to discuss them in your report.

Do not forget to reconnect the trigger and reconfigure TRB for cosmic data!

7.1.6. Data taking

With the settings chosen in the two previous tasks, a large dataset should be recorded over night.

- Verify again that you chose the settings according to the two preparation tasks.
- Configure TRB using the icon for cosmic data on the monitor
- Start a new data taking.

7.2. Day 2 – Analysis

Over the night, the experiment has taken a large dataset comprised of several hundred thousand events. The tasks of the second lab course day consist of preparing this data for analysis and evaluating the taken data on a statistical basis. Looking at the histograms from the first day, you see that the drift time distributions still vary in position compared to each other. To remove this issue the detector should be calibrated before starting data analysis.

7.2.1. Calibration Option I: Pulse and Front-End board calibration

Now use StyxM2C2 to create an output file, which is already calibrated with pulses. Use 300 000 events this time.

- Use the cosmic data that you took overnight.
- Perform the calibration using the StyxCalibration tool with algorithm CalibFE.
- Open the ROOT output file and have a look at the drift time distributions in **Uncalibrated/Straws**. What do you see now?
- Now look at the two-dimensional plots in the directory **Uncalibrated/Layers2D**. Describe what you notice, what is the difference to the previous file?
- Now have a look at the histograms in the directories **Calibrated/Straws** and **Calibrated/Layers2D**. What changed in the distributions?
- Save example plots to discuss them in your report.

7.2.2. Calibration Option II: Straw-by-straw calibration

Looking at the histograms from the first day, you see that the drift time distributions still vary in position compared to each other. To remove this issue, a straw-by-straw calibration can be applied which examines the drift time spectrum for each straw, finds its starting point and shifts the full distribution to start at zero time. It also finds straws and marks them as hot, dead or continuous if the distribution shows some problems. For further explanation see section A.4.

- Perform the calibration using the StyxCalibration tool, which is described in appendix A.4 for 300 000 events.
- Open the ROOT output file and have a look at the plots. You can go through the histograms and discuss what you see and how the distributions are changing for before and after calibration. If you have any questions, do not hesitate to ask your tutor. Do not forget to save some plots as an example for your report.
- In particular, have a look at the two-dimensional plots in the directory **Uncalibrated/Layers2D**. Describe what you see in the light of the two-dimensional drift time distributions you saw on day 1.
- Now have a look at the histograms in the directory **Calibrated/Layers2D**. What changed in the distributions? Save example plots to discuss them in your report.

7.2.3. Tracking analysis

With the improved drift time spectra after the calibration, it is now possible to reconstruct tracks in the events as described above. Central parameters of reconstructed objects are later analysed with statistical methods. The program used for these tasks is StyxLabCourse which is generated from the code that you will write. It controls the bulk event generation, reconstruction and loads your own analysis code to create plots. You can find a description on the code in appendix A.6.

- Reconstruct 200 000 events to have enough statistics while skipping the 300 000 events you have used for calibration to evade a bias. The reconstruction of events is CPU intensive and takes a while. Therefore a limit on the number of events is necessary. Use the option `-C` to include your calibration file in the reconstruction.
- Now it is time to analyse the reconstructed events. The program StyxLabCourse is generated by your own code. It controls the bulk event generation, reconstruction and loads your own analysis code to create plots. The code is written in C++, but you don't really need programming skills to modify the code. Your tutor will open the integrated development environment *Eclipse* for you, which serves as an editor and helps you with hints while writing code. The program StyxLabCourse consists of one source file with a main function, called labCourse.cpp, and a class, called `StudentAnalysis`. They are both described

in detail in Appendix A.6. You can start the program from your `build` directory using

```
./StyxLabCourse
```

You can modify and run the class StudentAnalysis to create the following plots. Best implement them one-by-one and test if they work.

- Plot the number of hits per straw for each layer. Compare the three layers of a module.
- Plot the number of hits per straw for each full module. Compare the top and the bottom module with each other.
- Look at the two-dimensional histogram of the number of hits over the number of tracks per event. What can you state about their relation?
- Filter the events for exactly one track and plot the angular distribution of all tracks.
- Scrutinize the angular distribution of the tracks found. Does it match the expectation? Which deviations do you see and how do you explain those?
- Plot the track angle against the segment angle for events with 1 track.

A. Software

Several software tools are provided to perform the required tasks of this lab course experiment. A short description of each tool is given in this section.

A.1. StyxM2C2

StyxM2C2 (Merge, Map, Calibrate and Convert) is the beginning of the analysis chain. It takes the files written by the readout system as input and produces output files that are needed for the subsequent process steps. As described in section 6 the recorded data has to undergo some processing steps to obtain usable drift time values. All those steps are executed by M2C2. By default two output files are produced, one of which contains the drift time measurements on straw level and one of which contains the pure time measurements on the level of the readout electronics.

StyxM2C2 supports various different options to customize the level of process steps applied:

-N <**MaxEvents**> Number of events to be processed. "-1" means all events

-C <**calibfile**> Giving a file here automatically applies a calibration

-S <**SkipEvents**> Number of events to skip.

-M <**Mapingfile**>

-O <**OutFile**> Name for the output file to be written

-I <**infile**> Path to a data file

−−merge / −−no-merge Merge / don't merge leading and trailing edges to hits

−−map / −−no-map Map / don't map TDC channels to front-end boards as defined in mapping file

−−clean / −−no-clean Clean / don't clean hits with non-nominal width

−−flip / −−no-flip Flip / don't flip leading and trailing edges as defined in the mapping file

−−reftime / −−no-reftime Subtract / don't subtract trigger reference time

−−demultiplex / −−no-demultiplex De-multiplex / don't demultiplex TDC hits into straw hits

−−all Apply all the above mentioned steps

−−pulse Apply all the steps needed for processing pulse calibration files

Typically you will only need a few of them. The explicit options for a given task during the lab course are discussed where needed.

M2C2 always produces two output files. When given e.g. `Test.txt` as output file name it will also produce a monitoring file named `Test_mon.txt`.

A.2. StyxMonitor

StyxMonitor analyses the monitoring files produced by M2C2 and writes a ROOT file. The program call `StyxMonitor Test_mon.txt` will produce a file `Test_mon.root` which can be viewed using ROOT, e.g. `root Test_mon.root`.

A.3. StyxThresholdScan

StyxThresholdScan produces overview plots from several monitoring files to help finding the right threshold setting for the front-end electronics. It compares one TDC channel across several files and displays the differences. Options are the TDC number, the channel number and a list of monitoring files. An example call would be

```
StyxThresholdScan 1 5 Run1_mon.txt Run2_mon.txt Run3_mon.txt
```

where Run1-3_mon.txt are datasets taken with different settings for the front-end threshold.

StyxThresholdScan generates a root file containing all plots and two pdf files with overview plots.

A.4. StyxCalibration

StyxCalibration is the tool of choice for calibrating all the straws of the experiment as well as flagging problematic straws. The calibration of the single straws is needed to properly convert measured drift times into radii in the experiment. For simplicity, the calibration also assigns a collective timing to the straws.

It can also happen, that straws constantly or randomly fire or don't fire at all. Such straws are found by the calibration routines and flagged to be handled appropriately.

Although the calibration code implements a larger number of methods, the usage is simple as a default is defined. You can run it and create a calibration file in the following way:

```
StyxCalibration -I myM2C2Output.txt -A CalibMethod
```

There are three different calibrations method in this lab.course. If you did not take any data with pulse generator, you have to use **CalibStrawByStraw**.

- CalibStrawByStraw: calibration is peformed for each straw individually
- CalibPulse: calibration of the electronic components of the experiment
- CalibFE: calibration applied to each front-end board. Only makes sense after performing pulse calibration

After running the program, corresponding output files will be created. For example, **SbSCalib.root** contains are large range of control plots while **SbSCalib.txt** is the file containing the calibration information which can be fed into the StyxM2C2 program to apply it to all measured hits. If you like, it is also possible to choose the output file name, just add **-O OutputFileName** to the previous command. You do not need any file extensions, ROOT and .TXT file will have same name.

A.5. StyxDisplay

To visualize the measured events and the result of the reconstruction, StyxDisplay is used. You can start it without any command line option. The program summons a graphical user interface that is divided into the event display on the right side and the task area on the left.

Data The first tab is still left empty intentionally. Implementation of data reconstruction will follow in the future.

Monte Carlo simulation (MC) This tab allows the creation and reconstruction of simulated events. You can specify the number of events, the number of generated tracks, the noise level and a smearing factor. The noise level adds random noisy straws to the event and the smearing alters the drift radii by a random factor which is picked from a Gaussian. Hitting the button starts the simulation. Mind that this can take a while if you simulate a large number of events and/or tracks.

Analysis (Analyse) This tab is not used in the lab course experiment.

Refit The refit tab allows to study the different segment finding and track fitting algorithms. You can remove the current reconstruction and rerun with a new configuration. There are two segment finders that use either 4 or 10 closest neighbours and two tracking algorithms. Algorithm A (blue) combines two segments into a track and algorithm B (pink) uses single segments to search for two compatible hits in the other module. Mind that you can enable and disable showing objects in the icon bar in the top left.

Events The last tab is used to browse through the events and to look at a certain event.

Mind that loading large files into the event display can take a while as all the events have to be loaded. While the program seems to be hanging, it is just loading all the data into memory, so please just be a bit patient or load a smaller file.

A.6. StyxLabCourse

A.6.1. StyxLabCourse main function

The main function consits of two larger code parts. The first part is used to process Monte Carlo simulation and the second part processes data taken by the experiment. The code relies on ROOT classes called `TTask`. In the example you can find tasks for simulation (`SSimulate`), reconstruction (`SBuildTaks`) and finally analysis (`StudentAnalysis`). The reconstruction and analysis codes are the same whether you have simulated events or data. Each task has a variety of settings, like input file names and output file name, number of events to process and others. You can run certain tasks in two ways:

- If you want to run only a single task once, you just execute StyxLabCourse and look in the `TBrowser` for your task in the tree on the left. Then right-click on the task and click `ExecuteTask`.
- If you want to run a task automatically, just add to the end of the task settings in the main function `anaData1->ExecuteTask()`.

A.6.2. StudentAnalysis

The class StudentAnalysis is defined in two files. A header file called `StudentAnalysis.h` and a source file called `StudentAnalysis.cxx`. You normally only need to edit the source file. The header file contains definitions of the class and functions. One such definition tells the compiler, that `StudentAnalysis` is a class looking like a `TTask`. In the source file, you will find two functions that you need to modify.

- `void StudentAnalysis::BookHistograms()` is where you create new plots. You can already find examples for histograms in this function which you can copy and change according to your needs. `TH1D` is a one-dimensional histogram, `TH2D` is a two-dimensional histogram. You can also set the axis titles here.
- `void StudentAnalysis::FillHistograms()` is where you can add entries to the histograms. This function is automatically executed once per event. You also find here examples how to fill histograms with one or two dimensions and also how to apply cuts (using an if-clause).

You can compile the code using the keys `CTRL+B`. You can also force the text completion using `CTRL+Space` which is helpful as it also shows you the code documentation. Don't hesitate to ask the tutor for more information.

B. Basics of data analysis using ROOT

The STYX analysis code heavily relies on ROOT, an open source data analysis framework based on the C++ programming language. It is a standard software for data analysis in many areas of particle physics. We want to give you an impression on the usage of ROOT here, as it is used in daily work in high-energy physics also here in Bonn. You can find out more about ROOT on the website: `http://root.cern.ch`. Here we will give some useful hints for your Styx analysis.

- To start ROOT in interactive mode, just execute the command `root` on the console.
- In interactive mode, you can open a file and object browser. Just use the command `new TBrowser` inside the ROOT shell.
- To quit the interactive shell, use the command `.q` followed by `Enter`.
- You can overlay histograms with the keyword *same* in the draw option text field at the top of the TBrowser.

- Two-dimensional histograms can be coloured writing the option *colz* into the same field before opening the histogram.

C. Literature about cosmic rays

From C. Grupen, “Astroparticle Physics”

$$\omega_f \approx \omega_i \frac{1-\cos\varphi_i}{1-\cos\varphi_f}\,, \tag{6.88}$$

where φ_i and φ_f are the angles between the incoming electron and the incoming and outgoing photon. The above approximation holds if $E_i \gg m_i \gg \omega_i$.

7. What is the temperature of a cosmic object if its maximum blackbody emission occurs at an energy of $E = 50\,\mathrm{keV}$?
(Hint: The solution of this problem leads to a transcendental equation which needs to be solved numerically.)

Problems for Sect. 6.5

1. A photon propagating to a celestial object of mass M will gain momentum and will be shifted towards the blue. Work out the relative gain of a photon approaching the Sun's surface from a height of $H = 1\,\mathrm{km}$. Analogously, a photon escaping from a massive object will be gravitationally redshifted.
(Radius of the Sun $R_\odot = 6.9635 \times 10^8\,\mathrm{m}$, Mass of the Sun $M_\odot = 1.993 \times 10^{30}\,\mathrm{kg}$, acceleration due to Sun's gravity $g_\odot = 2.7398 \times 10^2\,\mathrm{m/s^2}$.)
2. Accelerated masses radiate gravitational waves. The emitted energy per unit time is worked out to be

$$P = \frac{G}{5c^2}\,\dddot{Q}^2\,,$$

where Q is the quadrupole moment of a certain mass configuration (e.g., the system Sun–Earth). For a rotating system with periodic time dependence ($\sim \sin\omega t$) each time derivative contributes a factor ω, hence

$$P \approx \frac{G}{5c^2}\,\omega^6\,Q^2\,.$$

For a system consisting of a heavy-mass object like the Sun (M) and a low-mass object, like Earth (m), the quadrupole moment is on the order of mr^2. Neglecting numerical factors of order unity, one gets

$$P \approx \frac{G}{c^2}\,\omega^6\,m^2\,r^4\,.$$

Work out the power radiated from the system Sun–Earth and compare it with the gravitational power emitted from typical fast-rotating laboratory equipments.

7 Secondary Cosmic Rays

"There are more things in heaven and earth, Horatio, than are dreamt of in your philosophy."

Shakespeare, Hamlet

For the purpose of astroparticle physics the influence of the Sun and the Earth's magnetic field is a perturbation, which complicates a search for the sources of cosmic rays. The solar activity produces an additional magnetic field which prevents part of galactic cosmic rays from reaching Earth. Figure 7.1, however, shows that the influence of the Sun is limited to primary particles with energies below 10 GeV. The flux of low-energy primary cosmic-ray particles is anticorrelated to the solar activity.

solar modulation

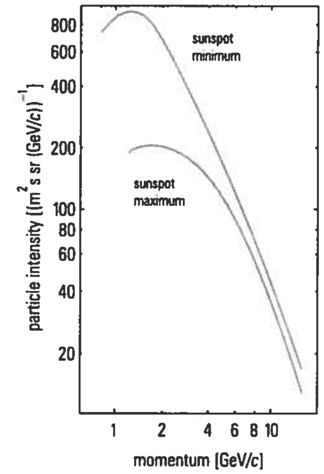

Fig. 7.1
Modulation of the primary spectrum by the 11-year cycle of the Sun

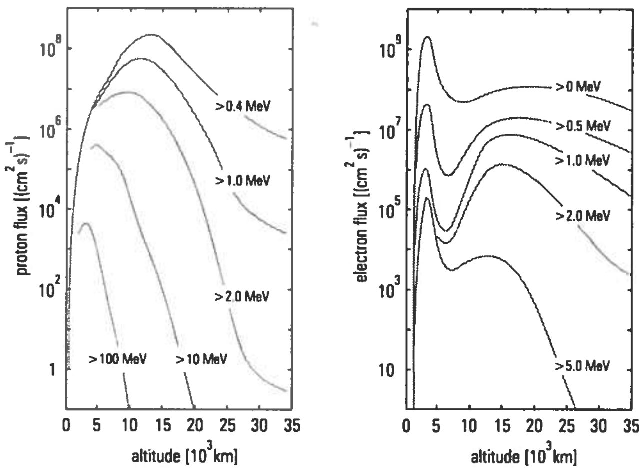

Fig. 7.2
Flux densities of protons and electrons in the radiation belts of the Earth

solar wind

On the other hand, the solar wind, whose magnetic field modulates primary cosmic rays, is a particle stream in itself, which can be measured at Earth. The particles constituting the solar wind (predominantly protons and electrons) are of low energy (MeV region). These particles are captured to a large extent by the Earth's magnetic field in the Van Allen belts or they are absorbed in the upper layers of the Earth's atmosphere (see Fig. 7.9). Figure 7.2 shows the flux den-

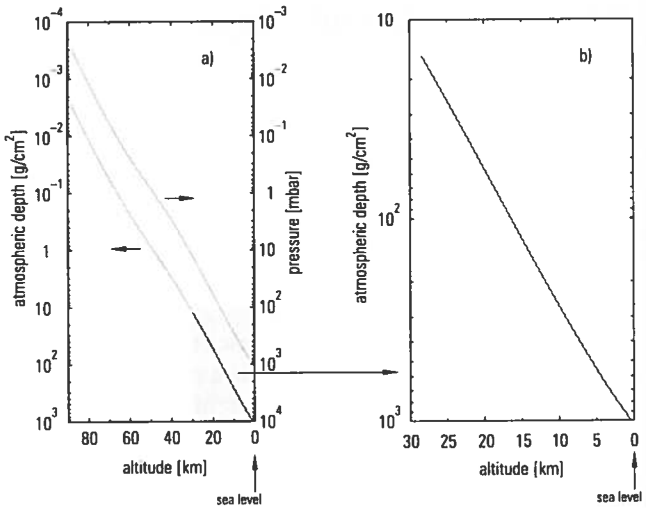

Fig. 7.3
(a) Relation between atmospheric depth (column density) and pressure
(b) column density of the atmosphere as a function of altitude up to 28 km

sities of protons and electrons in the Van Allen belts. The proton belt extends over altitudes from 2 000 to 15 000 km. It contains particles with intensities up to $10^8/(\mathrm{cm}^2\,\mathrm{s})$ and energies up to 1 GeV. The electron belt consists of two parts. The inner electron belt with flux densities of up to 10^9 particles per cm^2 and s is at an altitude of approximately 3 000 km, while the outer belt extends from about 15 000 km to 25 000 km. The inner part of the radiation belts is symmetrically distributed around the Earth while the outer part is subject to the influence of the solar wind and consequently deformed by it (see also Fig. 1.9 and Fig. 1.13).

radiation belts

7.1 Propagation in the Atmosphere

"Astroparticles are messengers from different worlds."

Anonymous

interaction in the atmosphere

Primary cosmic rays are strongly modified by interactions with atomic nuclei in the atmospheric air. The column density of the atmosphere amounts to approximately 1000 g/cm^2, corresponding to the atmospheric pressure of about 1000 hPa. Figure 7.3 (a) shows the relation between column density, altitude in the atmosphere, and pressure. Figure 7.3 (b) shows this relation in somewhat more detail for altitudes below 28 km. The residual atmosphere for flight altitudes

column density

of scientific balloons ($\approx$ 35–40 km) corresponds to approximately several g/cm^2. For inclined directions the thickness of the atmosphere increases strongly (approximately like $1/\cos\theta$, with θ – zenith angle). Figure 7.4 shows the variation of atmospheric depth with zenith angle at sea level.

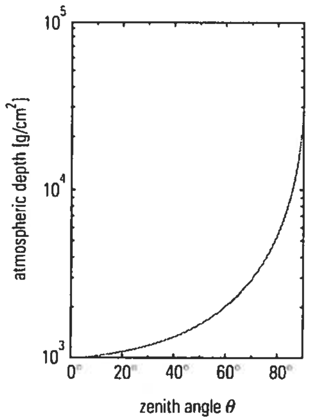

Fig. 7.4
Relation between zenith angle and atmospheric depth at sea level

For the interaction behaviour of primary cosmic rays the thickness of the atmosphere in units of the characteristic interaction length for the relevant particles species in question is important. The *radiation length* for photons and electrons in air is $X_0 = 36.66\,\mathrm{g/cm}^2$. The atmosphere therefore corresponds to a depth of 27 radiation lengths. The relevant *interaction length* for hadrons in air is $\lambda = 90.0\,\mathrm{g/cm}^2$, corresponding to 11 interaction lengths per atmosphere. This means that practically not a single particle of original primary cosmic rays arrives at sea level. Already at altitudes of 15 to 20 km primary cosmic rays interact with atomic nuclei of the air and initiate – depending on energy and particle species – electromagnetic and/or hadronic cascades.

radiation length

interaction length

electromagnetic and hadronic cascades

The momentum spectrum of the singly charged component of primary cosmic rays at the top of the atmosphere is shown in Fig. 7.5. In this diagram the particle velocity $\beta = v/c$ is shown as a function of momentum. Clearly visible are the bands of hydrogen isotopes as well as the low flux of primary antiprotons. Even at these altitudes several muons have been produced via pion decays. Since muon and pion mass are very close, it is impossible to separate them out in this scatter diagram. Also relativistic electrons and positrons would populate the bands labeled μ^+ and μ^-. One generally assumes that the measured antiprotons are not of primordial origin, but are rather produced by interactions in interstellar or interplanetary space or even in the residual atmosphere above the balloon.

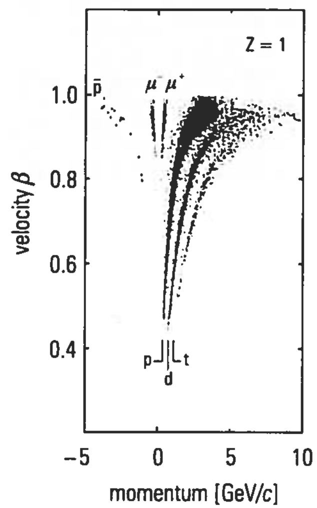

Fig. 7.5
Identification of singly charged particles in cosmic rays at a flight altitude of balloons ($\hat{=}$ 5 g/cm^2 residual atmosphere) [21]

The transformation of primary cosmic rays in the atmosphere is presented in Fig. 7.6. Protons with approximately 85% probability constitute the largest fraction of primary cosmic rays. Since the interaction length for hadrons is 90 g/cm^2, primary protons initiate a hadron cascade already in their first interaction approximately at an altitude corresponding to the 100 mbar layer. The secondary particles most copiously produced are pions. Kaons on the other hand are only produced with a probability of 10% compared to pions. Neutral pions initiate via their decay ($\pi^0 \to \gamma + \gamma$) electromagnetic cascades, whose development is characterized by the shorter radiation length ($X_0 \approx \frac{1}{3}\lambda$ in air). This

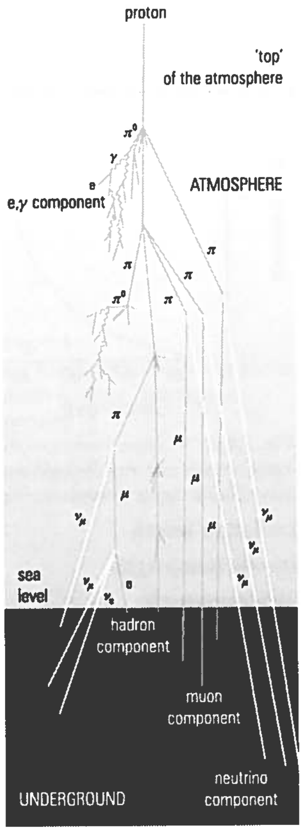

Fig. 7.6
Transformation of primary cosmic rays in the atmosphere

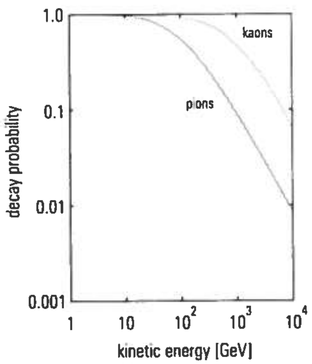

Fig. 7.7
Decay probabilities for charged pions and kaons in the atmosphere as a function of their kinetic energy

shower component is absorbed relatively easily and is therefore also named a soft component. Charged pions and kaons can either initiate further interactions or decay.

The competition between decay and interaction probability is a function of energy. For the same Lorentz factor charged pions (lifetime 26 ns) have a smaller decay probability compared to charged kaons (lifetime 12.4 ns). The decay probability of charged pions and kaons in the atmosphere is shown in Fig. 7.7 as a function of their kinetic energy. The leptonic decays of pions and kaons produce the penetrating muon and neutrino components ($\pi^+ \to \mu^+ + \nu_\mu$, $\pi^- \to \mu^- + \bar{\nu}_\mu$; $K^+ \to \mu^+ + \nu_\mu$, $K^- \to \mu^- + \bar{\nu}_\mu$). Muons can also decay and contribute via their decay electrons to the soft component and neutrinos to the neutrino component ($\mu^+ \to e^+ + \nu_e + \bar{\nu}_\mu$, $\mu^- \to e^- + \bar{\nu}_e + \nu_\mu$).

The energy loss of relativistic muons not decaying in the atmosphere is low ($\approx$ 1.8 GeV). They constitute with 80% of all charged particles the largest fraction of secondary particles at sea level.

Some secondary mesons and baryons can also survive down to sea level. Most of the low-energy charged hadrons observed at sea level are locally produced. The total fraction of hadrons at ground level, however, is very small.

Apart from their longitudinal development electromagnetic and hadronic cascades also spread out laterally in the atmosphere. The lateral size of an electromagnetic cascade is caused by *multiple scattering* of electrons and positrons, while in hadronic cascades the *transverse momenta* at production of secondary particles are responsible for the lateral width of the cascade. Figure 7.8 shows a comparison of the shower development of 100 TeV photons and 100 TeV protons in the atmosphere. It is clearly visible that transverse momenta of secondary particles fan out the hadron cascade.

The intensity of protons, electrons, and muons of all energies as a function of the altitude in the atmosphere is plotted in Fig. 7.9. The absorption of protons can be approximately described by an exponential function.

The electrons and positrons produced through π^0 decay with subsequent pair production reach a maximum intensity at an altitude of approximately 15 km and soon after are relatively quickly absorbed while, in contrast, the flux of muons is attenuated only relatively weakly.

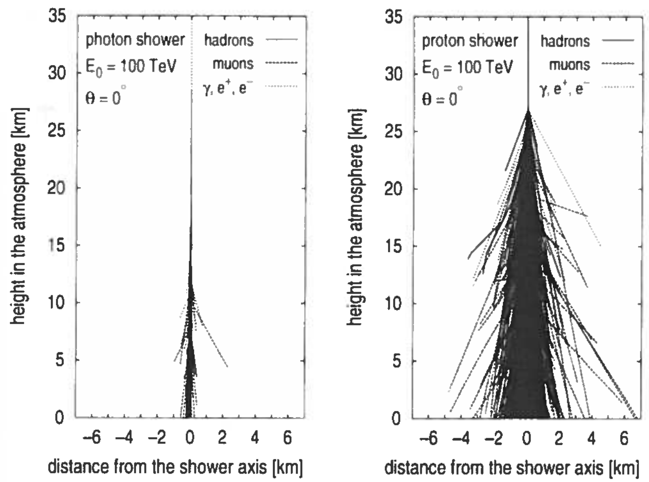

Fig. 7.8
Comparison of the development of electromagnetic (100 TeV photon) and hadronic cascades (100 TeV proton) in the atmosphere. Only secondaries with $E \geq 1$ GeV are shown [22]

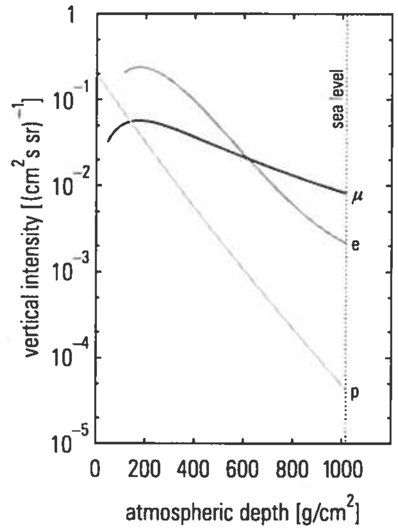

Fig. 7.9
Particle composition in the atmosphere as a function of atmospheric depth

Because of the steepness of the energy spectra the particle intensities are of course dominated by low-energy particles. These low-energy particles, however, are mostly of secondary origin. If only particles with energies in excess of 1 GeV are counted, a different picture emerges (Fig. 7.10).

sea-level composition

Primary nucleons (protons and neutrons) with the initial high energies dominate over all other particle species down to altitudes of 9 km, where muons take over. Because of the low interaction probability of neutrinos these particles are practically not at all absorbed in the atmosphere.

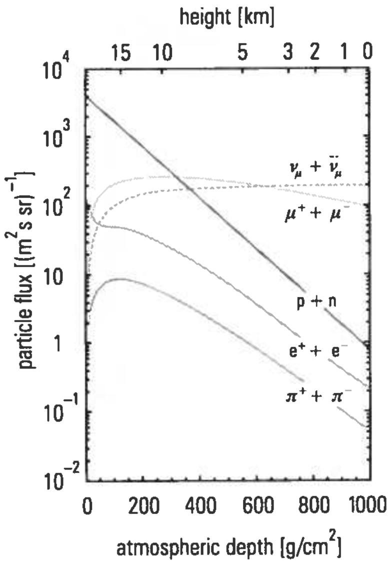

Fig. 7.10
Intensities of cosmic-ray particles with energies > 1 GeV in the atmosphere

Their flux increases monotonically because additional neutrinos are permanently produced by particle decays.

Since the energy spectrum of primary particles is relatively steep, the energy distribution of secondaries also has to reflect this property.

proton and muon spectra

Figure 7.11 shows the proton and muon spectra for various depths in the atmosphere. Clearly visible is the trend that with increasing depth in the atmosphere muons start to dominate over protons especially at high energies.

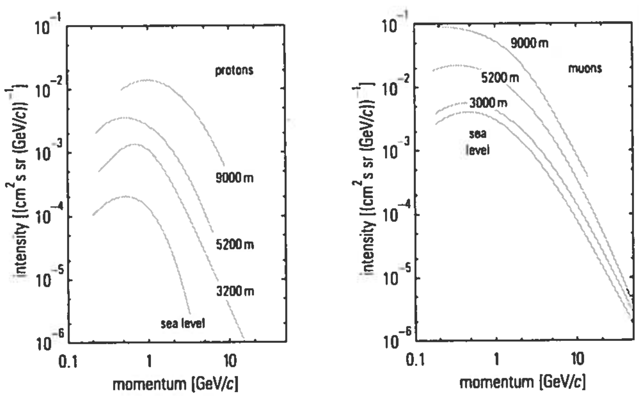

Fig. 7.11
Momentum spectra of protons and muons at various altitudes in the atmosphere

7.2 Cosmic Rays at Sea Level

"The joy of discovery is certainly the liveliest that the mind of man can ever feel."

Claude Bernard

A measurement of charged particles at sea level clearly shows that, apart from some protons, muons are the dominant component (Fig. 7.12).

Approximately 80% of the charged component of secondary cosmic rays at sea level are muons. Their flux through a horizontal area amounts to roughly one particle per cm^2 and minute. These muons originate predominantly from pion decays, since pions as lightest mesons are produced in large numbers in hadron cascades. The muon spectrum at sea level is therefore a direct consequence of the pion source spectrum. There are, however, several modifications. Figure 7.13 shows the parent pion spectrum at the location of production in comparison to the observed sea-level muon spectrum. The shape of the muon spectrum agrees relatively well with the pion spectrum for momenta between 10 and 100 GeV/c. For energies below 10 GeV and above 100 GeV the muon intensity, however, is reduced compared to the pion source spectrum. For low energies the muon decay probability is increased. A muon of 1 GeV with a Lorentz factor of $\gamma = E/m_\mu c^2 = 9.4$ has a mean decay length of

$$s_\mu \approx \gamma \tau_\mu c = 6.2\,\text{km} . \qquad (7.1)$$

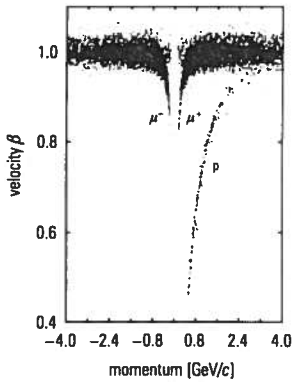

Fig. 7.12
Measurement and identification of charged particles at sea level [21]

Since pions are typically produced at altitudes of 15 km and decay relatively fast (for $\gamma = 10$ the decay length is only $s_\pi \approx \gamma \tau_\pi c = 78$ m), the decay muons do not reach sea level but rather decay themselves or get absorbed in the atmosphere. At high energies the situation is changed. For pions of 100 GeV ($s_\pi = 5.6$ km, corresponding to a column density of 160 g/cm^2 measured from the production altitude) the interaction probability dominates ($s_\pi > \lambda$). Pions of these energies will therefore produce further, tertiary pions in subsequent interactions, which will also decay eventually into muons, but providing muons of lower energy. Therefore, the muon spectrum at high energies is always steeper compared to the parent pion spectrum.

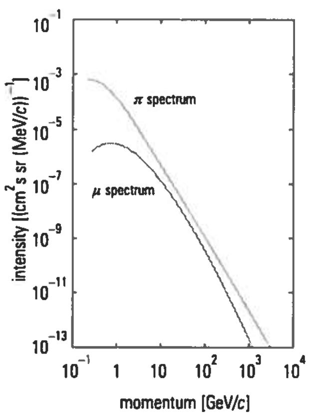

Fig. 7.13
Sea-level muon spectrum in comparison to the pion parent source spectrum at production

If muons from inclined horizontal directions are considered, a further aspect has to be taken into account. For large zenith angles the parent particles of muons travel relatively long distances in rare parts of the atmosphere. Because of the low area density at large altitudes for inclined directions the decay probability is increased compared to the interaction probability. Therefore, for inclined directions pions will produce predominantly high-energy muons in their decay.

muons from inclined directions

The result of these considerations is in agreement with observation (Fig. 7.14). For about $170\,\mathrm{GeV}/c$ the muon intensity at 83° zenith angle starts to outnumber that of the vertical muon spectrum. The intensity of muons from horizontal directions at low energies is naturally reduced because of muon decays and absorption effects in the thicker atmosphere at large zenith angles.

sea-level muon spectrum up to 20 TeV/c

The sea-level muon spectrum for inclined directions has been measured with solid-iron momentum spectrometers up to momenta of approximately $20\,\mathrm{TeV}/c$ (Fig. 7.15). For higher energies the muon intensity decreases steeply.

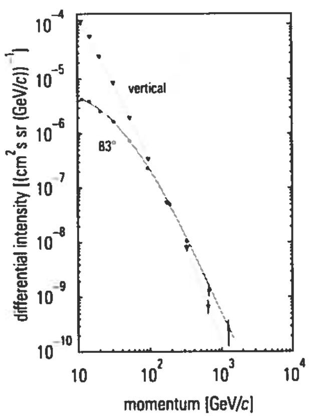

Fig. 7.14
Sea-level muon momentum spectra for vertical and inclined directions

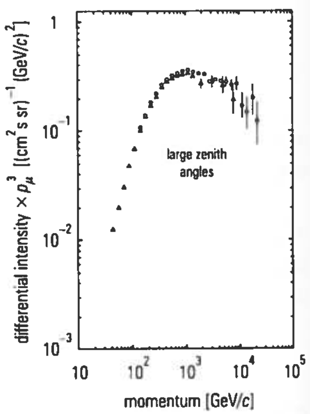

Fig. 7.15
Momentum spectrum of muons at sea level for large zenith angles. In this figure the differential intensity is multiplied by p_μ^3

The total intensity of muons, however, is dominated by low-energy particles. Because of the increased decay probability and the stronger absorption of muons from inclined directions, the total muon intensity at sea level varies like

$$I_\mu(\theta) = I_\mu(\theta = 0)\cos^n\theta \tag{7.2}$$

for not too large zenith angles θ. The exponent of the zenith-angle distribution is obtained to be $n = 2$. This exponent varies very little, even at shallow depths underground, if only muons exceeding a fixed energy are counted.

charge ratio of muons

An interesting quantity is the *charge ratio of muons* at sea level. Since primary cosmic rays are positively charged, this positive charge excess is eventually also transferred to

muons. If one assumes that primary protons interact with protons and neutrons of atomic nuclei in the atmosphere where the multiplicity of produced pions is usually quite large, the charge ratio of muons, $N(\mu^+)/N(\mu^-)$, can be estimated by considering the possible charge exchange reactions:

charge exchange reactions

$$\begin{aligned} p + N &\to p' + N' + k\pi^+ + k\pi^- + r\pi^0\,, \\ p + N &\to n + N' + (k+1)\pi^+ + k\pi^- + r\pi^0\,. \end{aligned} \tag{7.3}$$

In this equation k and r are the multiplicities of the produced particle species and N represents a target nucleon. If one assumes that for the reactions in (7.3) the cross sections are the same, the charge ratio of pions is obtained to be

$$R = \frac{N(\pi^+)}{N(\pi^-)} = \frac{2k+1}{2k} = 1 + \frac{1}{2k}\,. \tag{7.4}$$

For low energies $k = 2$ and thereby $R = 1.25$. Since this ratio is transferred to muons by the pion decay, one would expect a similar value for muons. Experimentally one observes that the charge ratio of muons at sea level is constant over a wide momentum range and takes on a value of

$$N(\mu^+)/N(\mu^-) \approx 1.27\,. \tag{7.5}$$

muons from semileptonic decays

In addition to 'classical' production mechanisms of muons by pion and kaon decays, they can also be produced in semileptonic decays of charmed mesons (for example, $D^0 \to K^-\mu^+\nu_\mu$ and $D^+ \to \bar{K}^0\mu^+\nu_\mu$, $D^- \to K^0\mu^-\bar{\nu}_\mu$). Since these charmed mesons are very short-lived ($\tau_{D^0} \approx 0.4\,\mathrm{ps}$, $\tau_{D^\pm} \approx 1.1\,\mathrm{ps}$), they decay practically immediately after production without undergoing interactions themselves. Therefore, they are a source of high-energy muons. Since the production cross section of charmed mesons in proton–nucleon interactions is rather small, D decays contribute significantly only at very high energies.

nucleon component

Figure 7.12 already showed that apart from muons also some nucleons can be observed at sea level. These nucleons are either remnants of primary cosmic rays, which, however, are reduced in their intensity and energy by multiple interactions, or they are produced in atmospheric hadron cascades. About one third of the nucleons at sea level are neutrons. The proton/muon ratio varies with the momentum of the particles. At low momenta ($\approx 500\,\mathrm{MeV}/c$) a p/μ ratio $N(p)/N(\mu)$ of about 10% is observed decreasing to larger momenta ($N(p)/N(\mu) \approx 2\%$ at $1\,\mathrm{GeV}/c$, $N(p)/N(\mu) \approx 0.5\%$ at $10\,\mathrm{GeV}/c$).

positrons, electrons, and photons from electromagnetic cascades

In addition to muons and protons, one also finds electrons, positrons, and photons at sea level as a consequence of the electromagnetic cascades in the atmosphere. A certain fraction of electrons and positrons originates from muon decays. Electrons can also be liberated by secondary interactions of muons ('knock-on electrons').

pions and kaons at sea level

The few pions and kaons observed at sea level are predominantly produced in local interactions.

production of ν_e and ν_μ

Apart from charged particles, electron and muon neutrinos are produced in pion, kaon, and muon decays. They constitute an annoying background, in particular, for neutrino astronomy. On the other hand, the propagation of atmospheric neutrinos has provided new insights for elementary particle physics, such as neutrino oscillations. A comparison of vertical and horizontal neutrino spectra (Fig. 7.16) shows a similar tendency as for muon spectra.

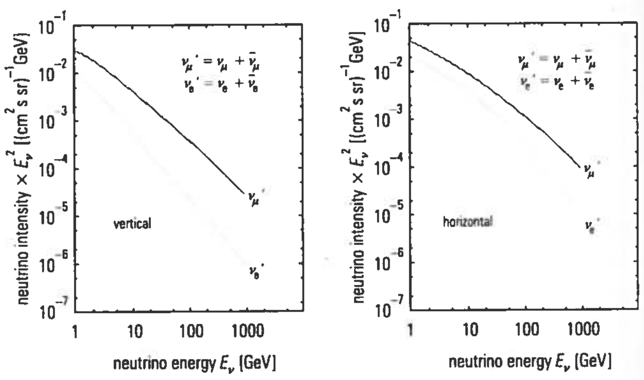

Fig. 7.16
Energy spectra of muon and electron neutrinos for vertical and horizontal directions

neutrino parents

Since the parent particles of neutrinos are dominantly pions and kaons and their decay probability is increased compared to the interaction probability at inclined directions, the horizontal neutrino spectra are also harder in comparison to the spectra from vertical directions. Altogether, muon neutrinos would appear to dominate, since the $(\pi \to e\nu)$ and $(K \to e\nu)$ decays are strongly suppressed due to *helicity conservation*. Therefore, pions and kaons almost exclusively produce muon neutrinos only. Only in muon decay equal numbers of electron and muon neutrinos are produced. At high energies also semileptonic decays of charmed mesons constitute a source for neutrinos.

dominance of ν_μ

Based on these 'classical' considerations the integral neutrino spectra yield a neutrino-flavour ratio of

$$\frac{N(\nu_\mu + \bar{\nu}_\mu)}{N(\nu_e + \bar{\nu}_e)} \approx 2 . \tag{7.6}$$

This ratio, however, is modified by propagation effects like neutrino oscillations (see Sect. 6.2: Neutrino Astronomy).

neutrino-flavour ratio

7.3 Cosmic Rays Underground

"If your experiment needs statistics, then you ought to have done a better experiment."

Ernest Rutherford

particle composition underground

Particle composition and energy spectra of secondary cosmic rays underground are of particular importance for neutrino astronomy. Experiments in neutrino astronomy are usually set up at large depths underground to provide a sufficient shielding against the other particles from cosmic rays. Because of the rarity of neutrino events even low fluxes of residual cosmic rays constitute an annoying background. In any case it is necessary to know precisely the identity and flux of secondary cosmic rays underground to be able to distinguish a possible signal from cosmic-ray sources from statistical fluctuations or systematical uncertainties of the atmospheric cosmic-ray background.

background sources for neutrino astrophysics

Long-range atmospheric muons, secondary particles locally produced by muons, and the interaction products created by atmospheric neutrinos represent the important background sources for neutrino astronomy.

energy loss of muons

Muons suffer energy losses by ionization, direct electron–positron pair production, bremsstrahlung, and nuclear interactions. These processes have been described in rather detail in Chap. 4. While the ionization energy loss at high energies is essentially constant, the cross sections for the other energy-loss processes increase linearly with the energy of the muon,

$$-\frac{\mathrm{d}E}{\mathrm{d}x} = a + b\,E . \tag{7.7}$$

range of muons

The energy loss of muons as a function of their energy is shown in Fig. 7.17 for iron as absorber material. The energy loss of muons in rock in its dependence on the muon energy was already shown earlier (Fig. 4.3).

Equation (7.7) allows to work out the range R of muons by integration,

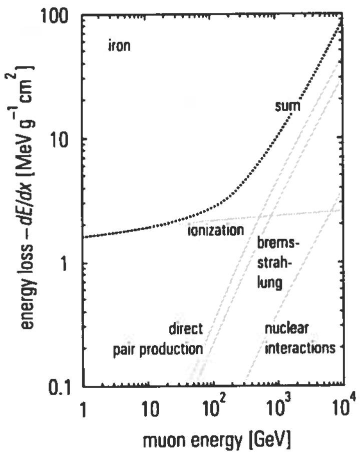

Fig. 7.17
Contributions to the energy loss of muons in iron

$$R = \int_E^0 \frac{dE}{-dE/dx} = \frac{1}{b}\ln(1 + \frac{b}{a}E) , \tag{7.8}$$

if it is assumed that the parameters a and b are energy independent.

For not too large energies ($E < 100\,\text{GeV}$) the ionization energy loss dominates. In this case $bE \ll a$ and therefore

$$R = \frac{E}{a} . \tag{7.9}$$

The energy loss of a *minimum-ionizing muon* in the atmosphere is

$$\frac{dE}{dx} = 1.82\,\text{MeV/(g/cm)}^2 . \tag{7.10}$$

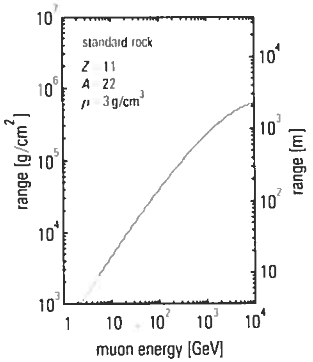

Fig. 7.18
Range of muons in rock

A muon of energy 100 GeV has a range of about 40 000 g/cm^2 in rock corresponding to 160 meter (or 400 meter water equivalent). An energy–range relation for standard rock is shown in Fig. 7.18. Because of the stochastic character of muon interaction processes with large energy transfers (e.g., bremsstrahlung) muons are subject to a considerable range straggling.

determination of the depth–intensity relation

The knowledge of the sea-level muon spectrum and the energy-loss processes of muons allow one to determine the *depth–intensity relation* for muons. The integral sea-level muon spectrum can be approximated by a power law

$$N(> E) = A\,E^{-\gamma} . \tag{7.11}$$

Using the energy–range relation (7.8), the depth–intensity relation is obtained,

$$N(> E, R) = A\left[\frac{a}{b}(e^{bR} - 1)\right]^{-\gamma} . \tag{7.12}$$

For high energies ($E_\mu > 1\,\text{TeV}$, $bE \gg a$) the exponential dominates and one obtains

$$N(> E, R) = A\left(\frac{a}{b}\right)^{-\gamma} e^{-\gamma bR} . \tag{7.13}$$

inclined muon directions

For inclined directions the absorbing ground layer increases like $1/\cos\theta = \sec\theta$ (θ – zenith angle) for a flat overburden, so that for muons from inclined directions one obtains a depth–intensity relation of

$$N(> E, R, \theta) = A\left(\frac{a}{b}\right)^{-\gamma} e^{-\gamma bR\sec\theta} . \tag{7.14}$$

For shallower depths (7.12), or also (7.9), however, leads to a power law

$$N(> E, R) = A\,(aR)^{-\gamma} . \tag{7.15}$$

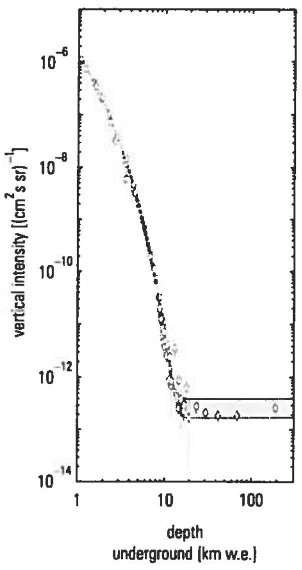

Fig. 7.19
Depth–intensity relation for muons from vertical directions. The *grey-hatched band* at large depths represents the flux of neutrino-induced muons with energies above 2 GeV (*upper line:* horizontal, *lower line:* vertical upward neutrino-induced muons) [2]

The measured depth–intensity relation for vertical directions is plotted in Fig. 7.19. From depths of 10 km water equivalent (≈ 4000 m rock) onwards muons induced by atmospheric neutrinos dominate the muon rate. Because of the low interaction probability of neutrinos the neutrino-induced muon rate does not depend on the depth. At large depths (> 10 km w.e.) a neutrino telescope with a collection area of 100 × 100 m^2 and a solid angle of π would still measure a background rate of 10 events per day.

The zenith-angle distributions of atmospheric muons for depths of 1500 and 7000 meter water equivalent are shown in Fig. 7.20. For large zenith angles the flux decreases steeply, because the thickness of the overburden increases

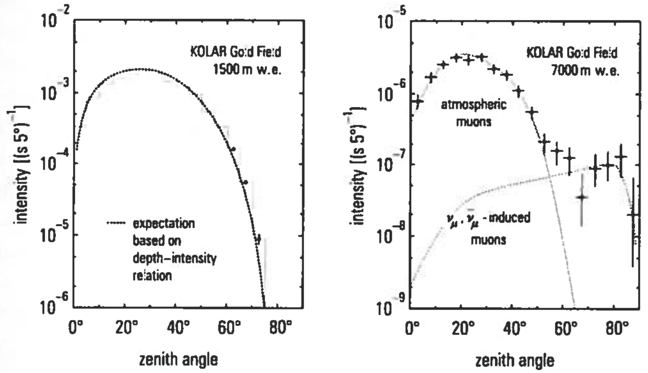

Fig. 7.20
Zenith-angle distribution of atmospheric muons at depths of 1500 and 7000 m w.e.

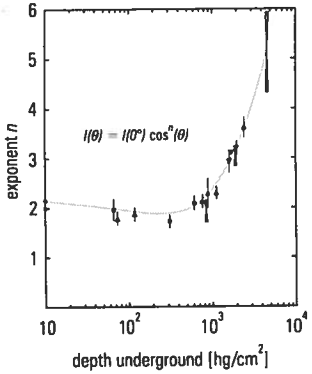

Fig. 7.21
Variation of the exponent n of the zenith-angle distribution of muons with depth

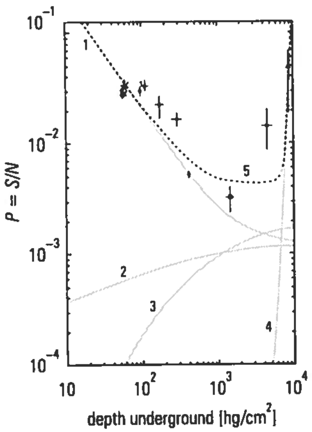

Fig. 7.22
Ratio of stopping to penetrating muons as a function of depth in comparison to some experimental results. (*1*) Stopping atmospheric muons, (*2*) stopping muons from nuclear interactions, (*3*) stopping muons locally produced by photons, (*4*) neutrino-induced stopping muons, and (*5*) sum of all contributions

like $1/\cos\theta$. Therefore, at large depths and from inclined directions neutrino-induced muons dominate.

For not too large zenith angles and depths the zenith-angle dependence of the integral muon spectrum can still be represented by

$$I(\theta) = I(\theta = 0)\cos^n\theta \tag{7.16}$$

(Fig. 7.21). For large depths the exponent n in this distribution, however, gets very large, so that it is preferable to use (7.14) instead.

The average energy of muons at sea level is in the range of several GeV. Absorption processes in rock reduce predominantly the intensity at low energies. Therefore, the average muon energy of the muon spectrum increases with increasing depth. Muons of high energy can also produce other secondary particles in local interactions. Since low-energy muons can be identified by their ($\mu \to e\nu\nu$) decay with the characteristic decay time in the microsecond range, the measurement of stopping muons underground provides an information about local production processes. The flux of stopping muons is normally determined for a detector thickness of $100\,\mathrm{g/cm^2}$ and the ratio P of stopping to penetrating muons is presented (Fig. 7.22).

A certain fraction of stopping muons is produced locally by low-energy pions which decay relatively fast into muons. Since the flux of penetrating muons decreases strongly with increasing depth, the ratio P of stopping to penetrating muons is dominated by neutrino interactions for depths larger than 5000 m w.e.

The knowledge of the particle composition at large depths below ground represents an important information for neutrino astrophysics.

Also remnants of extensive air showers, which developed in the atmosphere, are measured underground. Electrons, positrons, photons, and hadrons are completely absorbed already in relatively shallow layers of rock. Therefore, only muons and neutrinos of extensive air showers penetrate to larger depths. The primary interaction vertex of particles which initiate the air showers is typically at an atmospheric altitude of 15 km. Since secondary particles in hadronic cascades have transverse momenta of about $300\,\mathrm{MeV}/c$ only, the high-energy muons essentially follow the shower axis. For primaries of energy around 10^{14} eV lateral displacements of energetic muons ($\approx$ 1 TeV)

lateral spread of muons underground

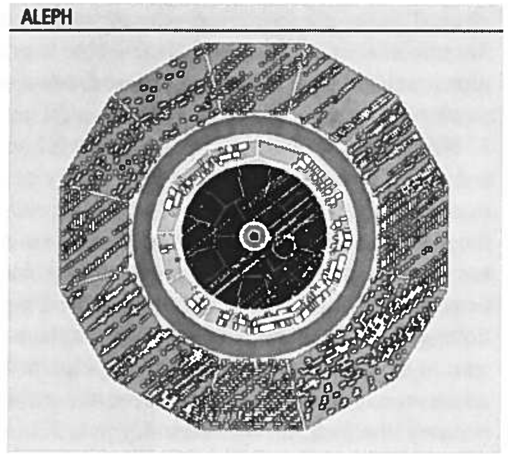

Fig. 7.23
Muon shower in the ALEPH experiment. Muon tracks are seen in the central time-projection chamber and in the surrounding hadron calorimeter. Even though there is a strong 1.5 Tesla magnetic field perpendicular to the projection shown, the muon tracks are almost straight indicating their high momenta. Only a knock-on electron produced in the time-projection chamber by a muon is bent on a circle [23]

at shallow depths underground of typically several meters exclusively caused by transferred transverse momenta are obtained. Typical multiple-scattering angles for energetic muons ($\approx$ 100 GeV) in thick layers of rock (50–100 m) are on the order of a few mrad.

muon bundles

The multiplicity of produced secondary particles increases with energy of the initiating particle (for a 1 TeV proton the charged multiplicity of particles for proton–proton interactions is about 15). Since the secondaries produced in these interactions decay predominantly into muons, one observes bundles of nearly parallel muons underground in the cores of extensive air showers. Figure 7.23 shows such a shower with more than 50 parallel muons observed by the ALEPH experiment at a depth of 320 m w.e.

ALEPH as cosmic-ray detector

High-energy muons are produced by high-energy primaries and, in particular, muon showers correlate with even higher primary energies. Therefore, one is tempted to localize extraterrestrial sources of high-energy cosmic rays via the arrival directions of single or multiple muons. Since Cygnus X3 has been claimed to emit photons with energies up to 10^{16} eV, this astrophysical source also represents an excellent candidate for the acceleration of high-energy charged primary cosmic rays. Cygnus X3 at a distance of approximately 33 000 light-years is an X-ray binary consisting of a superdense pulsar and a stellar companion. The material flowing from the companion into the direction of the pulsar forms an accretion disk around the pulsar. If apparently photons of very high energy can be produced, one would expect them to originate from the π^0 decay ($\pi^0 \to \gamma\gamma$).

Cygnus X3

Neutral pions are usually produced in proton interactions. Therefore, the source should also be able to produce charged pions and via their decay muons and muon neutrinos. Because of their short lifetime, muons would never survive the 33 000 light-year distance from Cygnus X3 to Earth, so that a possible muon signal must be caused by neutrino-induced muons. Unfortunately, muons and multi-muons observed in the Frejus experiment from the directions of Cygnus X3 are predominantly of atmospheric origin and do not confirm that Cygnus X3 is a strong source of high-energy particles (Fig. 7.24). The primary particles themselves accelerated in the source could in principle point back to the source when measured on Earth. However, the arrival direction of primary charged particles from Cygnus X3 could also have been completely randomized by the irregular galactic magnetic field. Muon production by neutrinos from Cygnus X3 would have been a rare event which would have required an extremely massive detector to obtain a significant rate.

Cygnus X3, a hadron accelerator?

muon astronomy

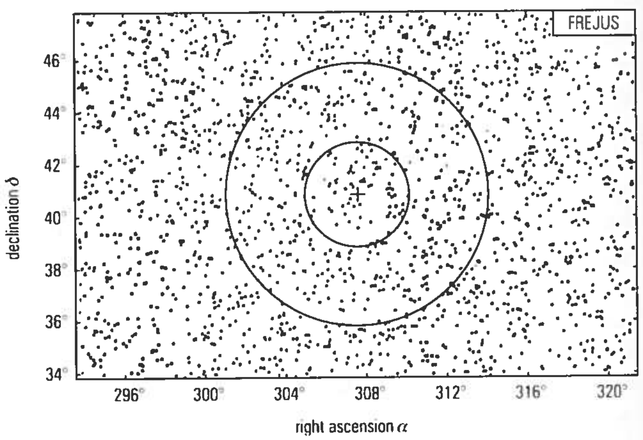

Fig. 7.24
Sky map of muons and multi-muons from the direction of Cygnus X3. The cross indicates the optically known position of Cygnus X3. The circles around Cygnus X3 with angles of ±2° and ±5° correspond to a possible fuzziness, caused by multiple scattering of muons in rock {24}

7.4 Extensive Air Showers

"Science never solves a problem without creating ten more."
George Bernard Shaw

Extensive air showers are cascades initiated by energetic primary particles which develop in the atmosphere. An extensive air shower (EAS) has an electromagnetic, a muonic, a

components of an extensive air shower

hadronic, and a neutrino component (see Fig. 7.6). The air shower develops a shower nucleus consisting of energetic hadrons, which permanently inject energy into the electromagnetic and the other shower components via interactions and decays. Neutral pions, which are produced in nuclear interactions and whose decay photons produce electrons and positrons via pair production, supply the electron, positron, and photon component. Photons, electrons, and positrons initiate electromagnetic cascades through alternating processes of pair production and bremsstrahlung. The muon and neutrino components are formed by the decay of charged pions and kaons (see also Fig. 7.6).

hadron, electromagnetic, muon, neutrino component

The inelasticity in hadron interactions is on the order of 50%, i.e., 50% of the primary energy is transferred into the production of secondary particles. Since predominantly pions are produced ($N(\pi) : N(K) = 9 : 1$) and all charge states of pions (π^+, π^-, π^0) are produced in equal amounts, one third of the inelasticity is invested into the formation of the electromagnetic component. Since most of the charged hadrons and the hadrons produced in hadron interactions also undergo multiple interactions, the largest fraction of the primary energy is eventually transferred into the electromagnetic cascade. Therefore, in terms of the number of particles, electrons and positrons constitute the main shower component. The particle number increases with shower depth t until absorptive processes like ionization for charged particles and Compton scattering and photoelectric effect for photons start to dominate and cause the shower to die out.

inelasticity

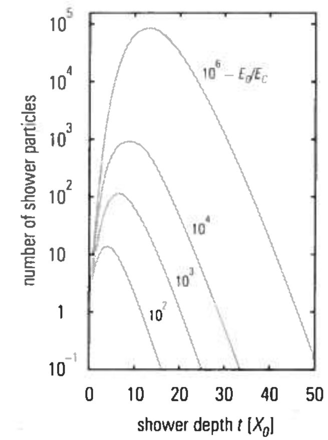

Fig. 7.25
Longitudinal shower development of electromagnetic cascades. (The critical energy in air is $E_c = 84$ MeV)

The development of electromagnetic cascades is shown in Fig. 7.25 for various primary energies. The particle intensity increases initially in a parabolical fashion and decays exponentially after the maximum of the shower has been reached. The longitudinal profile of the particle number can be parameterized by

$$N(t) \sim t^{\alpha} e^{-\beta t} , \tag{7.17}$$

where $t = x/X_0$ is the shower depth in units of the radiation length and α and β are free fit parameters. The position of the shower maximum varies only logarithmically with the primary energy, while the total number of shower particles increases linearly with the energy. The latter can therefore be used for the energy determination of the primary particle. One can imagine that the Earth's atmosphere represents a combined hadronic and electromagnetic calorimeter,

longitudinal particle-number profile

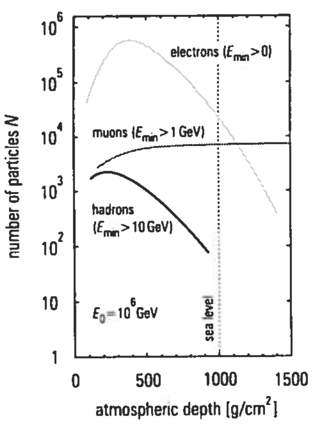

Fig. 7.26
Average longitudinal development of the various components of an extensive air shower in the atmosphere

in which the extensive air shower develops. The atmosphere constitutes approximately a target of 11 interaction lengths and 27 radiation lengths. The minimum energy for a primary particle to be reasonably well measured at sea level via the particles produced in the air shower is about 10^{14} eV = 100 TeV. As a rough estimate for the particle number N at sea level in its dependence on the primary energy E_0, one can use the relation

$$N = 10^{-10}\,E_0[\mathrm{eV}]\,. \tag{7.18}$$

Only about 10% of the charged particles in an extensive air shower are muons. The number of muons reaches a plateau already at an atmospheric depth of 200 g/cm^2 (see also Fig. 7.9 and Fig. 7.10). Its number is hardly reduced to sea level, since the probability for catastrophic energy-loss processes, like bremsstrahlung, is low compared to electrons because of the large muon mass. Muons also lose only a small fraction of their energy by ionization. Because of the relativistic time dilation the decay of energetic muons ($E_\mu > 3$ GeV) in the atmosphere is strongly suppressed.

longitudinal profile of a shower

Figure 7.26 shows schematically the longitudinal development of the various components of an extensive air shower in the atmosphere for a primary energy of 10^{15} eV.

lateral distribution

The lateral spread of an extensive air shower is essentially caused by the transferred transverse momenta in hadronic interactions and by multiple scattering of low-energy shower particles. The muon component is relatively flat compared to the lateral distribution of electrons and hadrons. Figure 7.27 shows the lateral particle profile for the various shower components. Neutrinos essentially follow the shape of the muon component.

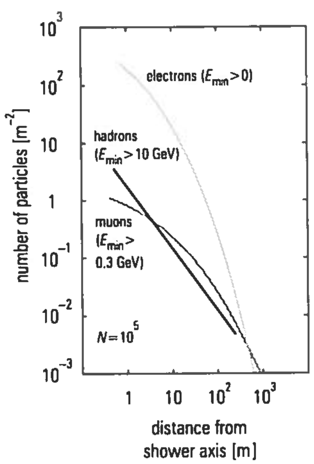

Fig. 7.27
Average lateral distribution of the shower components for $N = 10^5$ corresponding to $E \approx 10^{15}$ eV

Even though an extensive air shower initiated by primary particles with energies below 100 TeV does not reach sea level, it can nevertheless be recorded via the Cherenkov light emitted by the shower particles (see Sect. 6.3 on gamma-ray astronomy). At higher energies one has the choice of various detection techniques.

The classical technique for the measurement of extensive air showers is the sampling of shower particles at sea level with typically 1 m^2 large scintillators or water Cherenkov counters. This technique is sketched in Fig. 7.28.

Auger project

In the Auger project in Argentina 3000 sampling detectors will be used for the measurement of the sea-level component of extensive air showers. However, the energy assignment for the primary particle using this technique is not very

precise. The shower develops in the atmosphere which acts as a calorimeter of 27 radiation lengths thickness. The information on this shower is sampled in only *one*, the last layer of this calorimeter and the coverage of this layer is typically on the order of only 1%. The direction of incidence of the primary particle can be obtained from the arrival times of shower particles in the different sampling counters.

energy measurement

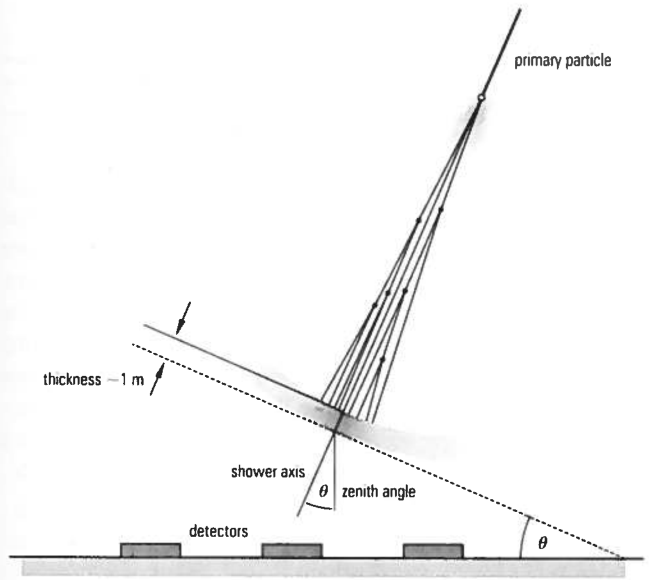

Fig. 7.28
Air-shower measurement with sampling detectors

Fly's Eye

It would be much more advantageous to measure the total longitudinal development of the cascade in the atmosphere. This can be achieved using the technique of the Fly's Eye (Fig. 7.29). Apart from the directional Cherenkov radiation the shower particles also emit an isotropic scintillation light in the atmosphere.

fluorescence technique

For particles with energies exceeding 10^{17} eV the fluorescence light of nitrogen is sufficiently intense to be recorded at sea level in the presence of the diffuse background of starlight. The actual detector consists of a system of mirrors and photomultipliers, which view the whole sky. An air shower passing through the atmosphere near such a Fly's Eye detector activates only those photomultipliers whose field of view is hit. The fired photomultipliers allow to reconstruct the longitudinal profile of the air shower. The total recorded light intensity is used to determine the shower energy. Such a type of detector allows much more

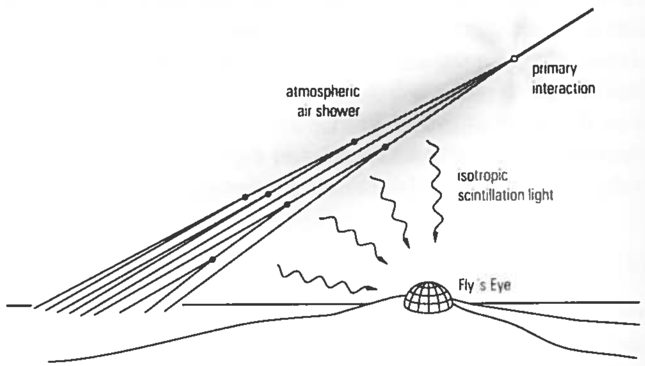

Fig. 7.29
Principle of the measurement of the scintillation light of extensive air showers

precise energy assignments, however, it has a big disadvantage compared to the classical air-shower technique that it can only be operated in clear moonless nights. Figure 7.30 shows an arrangement of mirrors and photomultipliers, as they have been used in the original Fly's Eye setup of the Utah group. In the Auger experiment the array of sampling detectors is complemented by such a number of telescopes which measure the scintillation light produced in the atmosphere. Much larger acceptances could be provided if such a Fly's Eye detector would be installed in orbit ('Air Watch', Fig. 7.31).

Air Watch

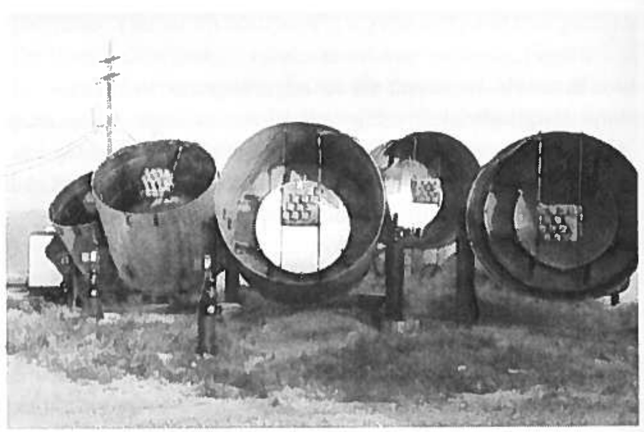

Fig. 7.30
Arrangement of mirrors and photomultipliers in the original Fly's Eye experiment of the Utah group [25]

radio detection of showers

Apart from these detection techniques it has also been tried to observe air showers via the electromagnetic radiation emitted in the radio band. It is generally believed that this radio signal is caused by shower electrons deflected in

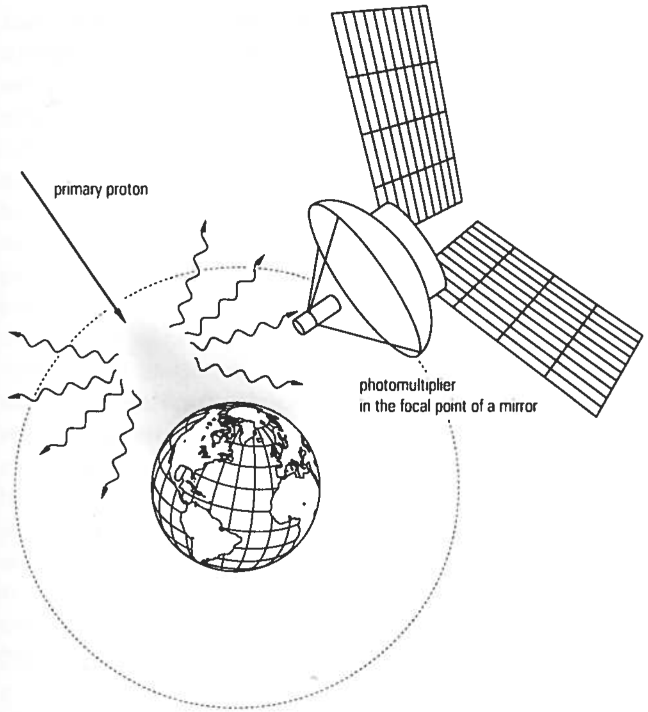

Fig. 7.31
Measurement of the isotropic scintillation light of extensive air showers by Fly's Eye detectors on board of satellites ('Air Watch')

the Earth's magnetic field thereby creating synchrotron radiation. Because of the strong background in practically all wavelength ranges these attempts have not been particularly successful so far. The possibility to detect large air showers via their muon content in underground experiments has been followed up in recent experiments.

muon showers underground

Apart from elementary particle physics aspects the purpose of the measurement of extensive air showers is the determination of the chemical composition of primary cosmic rays and the search for the sites of cosmic accelerators.

The arrival directions of the highest-energy particles ($> 10^{19}\,\mathrm{eV}$) which for intensity reasons can only be recorded via air-shower techniques, practically show no correlation to the galactic plane. This clearly indicates that their origin must be extragalactic. If the highest-energy primary cosmic-ray particles are protons, then their energies must be below $10^{20}\,\mathrm{eV}$, if they originate from distances of more than 50 Mpc. Even if their original energy were much higher, they would lose energy by photoproduction of pions on photons of the blackbody radiation until they fall below the threshold of the Greisen–Zatsepin–Kuzmin cutoff

proton horizon

($\approx 6 \times 10^{19}$ eV). Protons of this energy would point back to the sources, because galactic and intergalactic magnetic fields only cause angular distortions on the order of one degree at these high energies. The irregularities of magnetic fields, however, could lead to significant time delays between neutrinos and photons on one hand and protons, on the other hand, from such distant sources. This comes about because the proton trajectories are somewhat longer, even though their magnetic deflection is rather small. Depending on the distance from the source, time delays of months and even years can occur. This effect is of particular importance, if γ-ray bursters are also able to accelerate the highest-energy particles and if one wants to correlate the arrival times of photons from γ-ray bursts with those of extensive air showers initiated by charged primaries.

extensive air showers and γ-ray bursts

energies > 10^{20} TeV

The few measured particles with energies in excess of 10^{20} eV show a non-uniform distribution with a certain clustering near the local supergalactic plane. The fact that the attenuation length of protons with energies > 10^{20} eV in the intergalactic space is approximately 10 Mpc would make an origin in the local supercluster (maximum size 30 Mpc) plausible.

particle astronomy?

Out of the six measured showers with primary energy exceeding 10^{20} eV the directions of origin for two events are identical within the measurement accuracy. This direction coincides with the position of a radio galaxy (3C134), whose distance unfortunately is unknown, since it lies in the direction of the galactic plane, where optical measurements of extragalactic objects are difficult because of interstellar absorption. The coincidence of the radio galaxy 3C134 with the arrival directions of the two highest-energy particles can, of course, also be an accident.

coincidences over large distances

Normal extensive air showers have lateral widths of at most 10 km, even at the highest energies. However, there are indications that *correlations between arrival times* of air showers over distances of more than 100 km exist. Such coincidences could be understood by assuming that energetic primary cosmic particles undergo interactions or fragmentations at large distances from Earth. The secondary particles produced in these interactions would initiate separate air showers in the atmosphere (Fig. 7.32).

Even moderate distances of only one parsec (3×10^{16} m) are sufficient to produce separations of air showers at Earth on the order of 100 km (primary energy 10^{20} eV, transverse momenta $\approx 0.3\,\mathrm{GeV}/c$). Variations in arrival times of these showers could be explained by unequal energies of the fragments which could cause different propagation times. Galactic or extragalactic magnetic fields could also affect the trajectories of the fragments in a different way thus also influencing the arrival times.

correlated showers

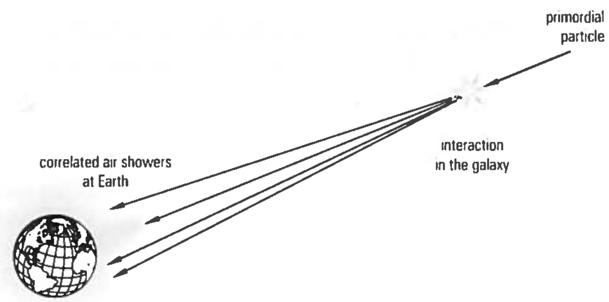

Fig. 7.32
Possible explanation for correlations between distant extensive air showers

7.5 Nature and Origin of the Highest-Energy Cosmic Rays

"The universe is full of magical things patiently waiting for our wits to grow sharper."

Eden Phillpotts

As already explained in Sect. 7.4, the highest-energy particles of cosmic rays appear to be of extragalactic origin. The problem of the sources of these particles is closely related to the identity of these particles. Up to the present time one had always assumed that the chemical composition of primary cosmic rays might change with energy. However, one always anticipated that the highest-energy particles were either protons, light, or possibly medium heavy nuclei (up to iron). For particles with energies exceeding 10^{20} eV this problem is completely open. In the following the candidates which might be responsible for cosmic-ray events with energies > 10^{20} eV will be critically reviewed.

identity of high-energy primaries?

Up to now only a handful of events with energies exceeding 10^{20} eV have been observed. Due to the measurement technique via extensive-air-shower experiments the energy assignments are connected with an experimental error of typically $\pm 30\%$. For the accelerated parent particles

events with $E > 10^{20}$ eV

of these high-energy particles the gyroradii must be smaller than the size of the source. Therefore, one can derive from

$$\frac{mv^2}{R} \leq evB$$

galactic containment

a maximum value for the energy of a particle that can be accelerated in the source,

$$E_{\max} \approx p_{\max} \leq eBR \tag{7.19}$$

(v is a particle velocity, B is a magnetic field strength of the source, R is the size of the source, m is the relativistic mass of the particle). In units appropriate for astroparticle physics the maximum energy, which can be obtained by acceleration in the source, can be expressed in the following way:

$$E_{\max} = 10^5\,\text{TeV}\,\frac{B}{3\times10^{-6}\,\text{G}}\,\frac{R}{50\,\text{pc}}\,. \tag{7.20}$$

With a typical value of $B = 3\,\mu\text{G}$ for our Milky Way and the very generous gyroradius of $R = 5$ kpc one obtains

$$E_{\max} = 10^7\,\text{TeV} = 10^{19}\,\text{eV}\,. \tag{7.21}$$

This equation implies that our Milky Way can hardly accelerate or store particles of these energies, so that for particles with energies exceeding 10^{20} eV one has to assume that they are of extragalactic origin.

protons

For protons the Greisen–Zatsepin–Kuzmin cutoff (GZK) of photoproduction of pions off blackbody photons through the Δ resonance takes an important influence on the propagation,

$$\gamma + p \rightarrow p + \pi^0\,. \tag{7.22}$$

The energy threshold for this process is at 6×10^{19} eV (see Sect. 6.1). Protons exceeding this energy lose rapidly their energy by such photoproduction processes. The mean free path for photoproduction is calculated to be

mean free path of protons

$$\lambda_{\gamma p} = \frac{1}{N\sigma}\,, \tag{7.23}$$

where N is the number density of blackbody photons and $\sigma(\gamma p \rightarrow \pi^0 p) \approx 100\,\mu\text{b}$ the cross section at threshold. This leads to

$$\lambda_{\gamma p} \approx 10\,\text{Mpc}\,. \tag{7.24}$$

Markarian galaxies as cosmic-ray source?

The Markarian galaxies Mrk 421 and Mrk 501, which have been shown to be sources of photons of the highest energies, would be candidates for the production of high-energy protons. Since they are residing at distances of approximately 100 Mpc, the arrival probability of protons from these distances with energies exceeding 10^{20} eV, however, is only

$$\approx e^{-x/\lambda} \approx 4 \times 10^{-5}\,. \tag{7.25}$$

Therefore protons can initiate the high-energy air-shower events only if they come from relatively nearby sources (i.e., from a local GZK sphere defined by distances < 30 Mpc, i.e., several mean free paths). The giant elliptical galaxy M87 lying in the heart of the Virgo cluster (distance ≈ 20 Mpc) is one of the most remarkable objects in the sky. It meets all of the conditions for being an excellent candidate for a high-energy cosmic-ray source.

M87 as particle accelerator?

It is, however, possible to shift the effect of the Greisen–Zatsepin–Kuzmin cutoff to higher energies by assuming that primary particles are nuclei. Since the threshold energy must be available per nucleon, the corresponding threshold energy, for example, for carbon nuclei ($Z = 6$, $A = 12$) would be correspondingly higher,

GZK sphere

$$E = E^p_{\text{cutoff}}\,A = 7.2 \times 10^{20}\,\text{eV}\,, \tag{7.26}$$

heavy nuclei

so that the observed events would not be in conflict with the Greisen–Zatsepin–Kuzmin cutoff. It is, however, difficult to understand, how atomic nuclei can be accelerated to such high energies, without being disintegrated by photon interactions or by fragmentation or spallation processes.

photo disintegration

One remote and rather drastic assumption to explain the trans-GZK events would be a possible violation of Lorentz invariance. If Lorentz transformations would not only depend on the relative velocity difference of inertial frames, but also on the absolute velocities, the threshold energy for γp collisions for interactions of blackbody photons with high-energy protons would be washed out and different from γp collisions when photon and proton had comparable energies, thus evading the GZK cutoff.

photons

Photons as possible candidates for the observed high-energy cascades are even more problematic. Because of the process of pair production of electrons and positrons off blackbody photons (see Sect. 6.3.3), photons have a relatively short mean free path of

mean free path of photons

$$\lambda_{\gamma\gamma} \approx 10\,\text{kpc}\,. \tag{7.27}$$

The γ-ray sources have to be relatively near to explain the high-energy showers. This would mean that they must be of galactic origin, which appears rather unlikely, because of the limited possibility for their parent particles to be accelerated in our Milky Way up to the highest energies required. High-energy photons, furthermore, would initiate air showers at high altitudes above sea level ($\approx$ 3000 km) due to interactions with the Earth's magnetic field. Therefore one would theoretically expect that they would reach a shower maximum at $\approx$ 1075 g/cm^2 (calculated from sea level). The event observed by the Fly's Eye experiment has a shower maximum at (815 ± 40) g/cm^2, which is typical for a hadron-induced cascade. Photons as candidates for the highest-energy events can therefore be firmly excluded.

photonic origin?

neutrinos

Recently, neutrinos were discussed as possible candidates for the high-energy events. But neutrinos also encounter severe problems in explaining such events. The ratio of the interaction cross section for neutrino–air and proton–air interactions at 10^{20} eV is

$$\left.\frac{\sigma(\nu\text{–air})}{\sigma(p\text{–air})}\right|_{E\approx 10^{20}\,\text{eV}} \approx 10^{-6}\,. \tag{7.28}$$

Quite enormous neutrino fluxes are required to explain the events with energies $> 10^{20}$ eV. It has been argued that the measurements of the structure function of the protons at HERA[1] have shown that protons have a rich structure of partons at low x ($x = E_{\text{parton}}/E_{\text{proton}}$). Even in view of these results showing evidence for a large number of gluons in the proton, one believes that the neutrino interaction cross section with nuclei of air cannot exceed 0.3 µb. This makes interactions of extragalactic neutrinos in the atmosphere very improbable, compare (3.56):

rising neutrino cross section?

$$\begin{aligned}\phi &= \sigma(\nu\text{–air})\,\frac{N_\text{A}}{A}\,d\\ &\le 0.3\,\mu\text{b}\,\frac{6\times 10^{23}}{14}\,\text{g}^{-1}\times 1000\,\text{g/cm}^2\\ &\approx 1.3\times 10^{-5}\end{aligned} \tag{7.29}$$

(N_A is the Avogadro number, d is a column density of the atmosphere).

[1] HERA – Hadron Elektron Ring Anlage at the Deutsches Elektronensynchrotron (DESY) in Hamburg

To obtain a reasonable interaction rate only neutrino interactions for inclined directions of incidence or in the Earth can be considered. The resulting expected distribution of primary vertices due to neutrino interactions is in contrast to observation. Therefore, neutrinos as well can very likely be excluded as candidates for the highest-energy cosmic air-shower events.

vertex distribution for neutrinos

WIMPs

It has been demonstrated that a large fraction of matter is in the form of dark matter. A possible way out concerning the question of high-energy particles in cosmic rays would be to assume that weakly interacting massive particles (WIMPs) could also be responsible for the observed showers with energies $> 10^{20}$ eV. It has to be considered that all these particles have only weak or even superweak interactions so that their interaction rate can only be on the order of magnitude of neutrino interactions.

The events with energies exceeding 10^{20} eV therefore represent a particle physics dilemma. One tends to assume that protons are the favoured candidates. They must come from relative nearby distances (< 30 Mpc), because otherwise they would lose energy by photoproduction processes and fall below the energy of 6×10^{19} eV. It is, however, true that up to these distances there are quite a number of galaxies (e.g., M87). The fact that the observed events do not clearly point back to a nearby source can be explained by the fact that the extragalactic magnetic fields are so strong that the directional information can be lost, even if the protons are coming from comparably close distances. Actually, there are hints showing that these fields are more in the µGauss rather than in the nGauss region [6].

extragalactic magnetic fields

Recent measurements, however, appear to indicate that the GZK cutoff might have been seen at least in the data of the HiRes experiment (see Fig. 6.5). On the other hand, this finding is in conflict with results from the large AGASA air-shower array (see also the comment on page 83).

acceleration mechanisms

Presently one assumes that in supernova explosions particles can only be accelerated to energies of 10^{15} eV by shock-wave mechanisms. At these energies the primary spectrum gets steeper ('knee of the primary spectrum'). As already shown, our Milky Way is too small to accelerate and store particles with energies exceeding 10^{20} eV. Furthermore, the arrival directions of the high-energy particles show practically no correlation to the galactic plane. Therefore, one has to assume that they are of extragalactic origin.

active galactic nuclei
blazars

Active galactic nuclei (AGN's) are frequently discussed as possible sources for the highest cosmic-ray energies. In this group of galaxies *blazars* play an outstanding rôle. Blazar is a short for sources belonging to the class of BL-Lacertae objects and quasars. BL-Lacertae objects, equally as quasars, are Milky Way-like sources, whose nuclei outshine the whole galaxy making them to appear like stars. While the optical spectra of quasars exhibit emission and absorption lines, the spectra of BL-Lacertae objects show no structures at all. This is interpreted in such a way that the galactic nuclei of quasars are surrounded by dense gas, while BL-Lacertae objects reside in low-gas-density elliptical galaxies.

BL-Lacertae objects, quasars

A characteristic feature of blazars is their high variability. Considerable brightness excursions have been observed on time scales as short as a few days. Therefore, these objects must be extremely compact, because the size of the sources can hardly be larger than the time required for light to travel across the diameter of the source. It is generally assumed that blazars are powered by black holes at their center. The matter falling into a black hole liberates enormous amounts of energy. While in nuclear fission only 1‰ and in nuclear fusion still only 0.7% of the mass is transformed into energy, an object of mass m can practically liberate all its rest energy mc^2 if it is swallowed by a black hole.

energy conversion efficiency

Many high-energy γ-ray sources which were found by the CGRO (Compton Gamma Ray Observatory) satellite, could be correlated with blazars. This led to the conjecture that these blazars could also be responsible for the acceleration of the highest-energy particles. The *particle jets* produced by blazars exhibit magnetic fields of more than 10 Gauss and extend over 10^{-2} pc and more. Therefore, according to (7.20), particles could be accelerated to energies exceeding 10^{20} eV. If protons are accelerated in such sources they could easily escape from these galaxies, because their interaction strength is smaller than that of the electrons which must certainly be accelerated as well. If these arguments are correct, blazars should also be a rich source of high-energy neutrinos. This prediction can be tested with the large water (or ice) Cherenkov counters.

particle jets from blazars

It has already been mentioned before that for protons to arrive at Earth the sources must not be at too large distances. The best candidates for sources should therefore lie in the supergalactic plane. The local supergalaxy is a kind of

supergalactic origin?

'Milky Way' of galaxies whose center lies in the direction of the Virgo cluster. The local group of galaxies, of which our Milky Way is a member, has a distance of about 20 Mpc from the center of this local supergalaxy and the members of this supergalaxy scatter around the supergalactic center only by about 20 Mpc.

Virgo cluster

Even though the origin of the highest-energy cosmic rays is still unknown, there are some hints that the sources for these high-energy events really lie in the supergalactic plane. Certainly more events are required to confirm in detail that such a correlation really exists. The Auger experiment under construction in Argentina should be able to solve the question of the origin of high-energy cosmic rays.

Finally, ideas have also been put forward that the extreme-energy cosmic rays are not the result of the acceleration of protons or nuclei but rather decay products of unstable primordial objects. Candidates discussed as possible sources are decays of massive GUT particles spread through the galactic halo, topological defects produced in the early stages of the universe like domain walls, 'necklaces' of magnetic monopoles connected by cosmic strings, closed cosmic loops containing a superconducting circulating current, or cryptons – relic massive metastable particles born during cosmic inflation.

exotic candidates

7.6 Problems

1. The pressure at sea level is 1013 hPa. Convert this pressure into a column density in kg/cm^2!
2. The barometric pressure varies with altitude h in the atmosphere (assumed to be isothermal) like

$$p = p_0 \, e^{-h/7.99\,\mathrm{km}} \, .$$

   What is the residual pressure at 20 km altitude and what column density of residual gas does this correspond to?
3. For not too large zenith angles the angular distribution of cosmic-ray muons at sea level can be parameterized as $I(\theta) = I(0)\cos^2\theta$. Motivate the $\cos^2\theta$ dependence!
4. Figure 7.22 shows the rate of stopping muons underground. Work out the rate of stopping atmospheric muons (curve labeled 1) as a function of depth underground for shallow depths!